Advanced short-wavelength infrared range-gated imaging for ground applications in monostatic and bistatic configurations

Endre Repasi,[1] Peter Lutzmann,[1] Ove Steinvall,[2,*] Magnus Elmqvist,[2] Benjamin Göhler,[1] and Gregor Anstett[1]

[1]Fraunhofer FOM, Research Institute for Optronics and Pattern Recognition, 76275 Ettlingen, Gutleuthausstrasse 1, Germany

[2]FOI, Swedish Defence Research Agency, P.O. Box 1165, 581 11 Linköping, Sweden

*Corresponding author: oveste@foi.se

Received 11 May 2009; revised 1 October 2009; accepted 2 October 2009; posted 6 October 2009 (Doc. ID 111242); published 23 October 2009

Some advanced concepts for gated viewing are presented, including spectral diversity illumination techniques, non-line-of-sight imaging, indirect scene illumination, and in particular setups in bistatic configurations. By using a multiple-wavelength illumination source target speckles could be substantially reduced, leading to an improved image quality and enhanced range accuracy. In non-line-of-sight imaging experiments we observed the scenery through the reflections in a window plane. The scene was illuminated indirectly as well by a diffuse reflection of the laser beam at different nearby objects. In this setup several targets could be spotted, which, e.g., offers the capability to look around the corner in urban situations. In the presented measuring campaigns the advantages of bistatic setups in comparison with common monostatic configurations are discussed. The appearance of shadows or local contrast enhancements as well as the mitigation of retroreflections supports the human observer in interpreting the scene. Furthermore a bistatic configuration contributes to a reduced dazzling risk and to observer convertness. © 2009 Optical Society of America

OCIS codes: 110.6150, 280.3420.

1. Introduction

Range-gated imaging has been discussed and demonstrated for a number of years and has in many cases reached close to operational status. Important work in the USA includes both unmanned ground vehicles [1] and airborne applications [2], both for long-range target identification and geolocation. The United Kingdom and France also have studied range-gated imaging (often referred to as burst illumination) for airborne and ground applications. Work on range-gated imaging has also been performed in Canada both for underwater imaging [3] and for long-range surveillance [4]. In Russia commercial range-gated cameras are manufactured by the company TURN Ltd. [5] for both underwater and land observation applications. An overview of range-gated imaging at FOI (Swedish Defence Research Agency)[6] was recently published including both land and underwater applications.

The main advantages of range-gated imaging include long-range target recognition, and difficult target recognition looking through camouflage, vegetation, water, haze and fog, fire, and smoke by using the range segmentation to separate the target from the background. An other important feature is the reduction of the influence of parasitic light such as the Sun and car lights. There are a large number of applications for gated viewing (GV) especially in combination with passive electro-optics or radar for target cuing and range gating for target

0003-6935/09/315956-14$15.00/0

classification. Complementing existing targeting devices equipped with laser range finders or designators with a range-gated imaging capability seems attractive, but also new compact handheld equipments in the form of binoculars may have an interesting potential in a number of applications. Combinations with thermal cameras result in systems with longer recognition ranges for the same optical aperture and often provide better target–background contrast (by range gating using silhouettes etc.) and images that are easier to interpret than pure thermal ones. New dual-mode detectors from SELEX S&AS, based on HgCdTe technology offer both capabilities. The same focal plane array can be switched to operate as a passive sensor in the mid-wavelengh IR or as a GV sensor in the short-wavelength IR (SWIR) [7]. The gated systems may also be used as single sensors for target tracking and classification, for example, against reflecting targets such as optics [8] and/or for shorter-range applications where a wider beam can be used as a search light, e.g., to look into buildings and cars. Navigation, surveillance, and search and rescue [9], especially looking against a sea or snow background [10], are other interesting applications due to the strong absorption at 1.5 μm. The performance of range-gated systems is limited by the sensor parameters as well as by target and atmospheric induced speckles [11], beam wander, and image dancing [12]. Close to the range limit the shot noise limits the image quality. Frame-to-frame integration is often used for reducing the scintillation and target speckle effects, in which case the image dancing and atmospheric coherence time become of importance. A spectrally broad emitting laser can also be used to reduce speckle effects. Range resolved (3D) images can be reconstructed from several frames by using sliding time gates [13–15]. The range accuracy and resolution for this depends on the single frame noise as well as the image dancing and beam wander. Performance modeling of range-gated systems is discussed by other authors [16–19].

A few years ago FGAN-FOM (Fraunhofer FOM) in Germany and FOI in Sweden acquired range-gated cameras working in the SWIR domain from the U.S. company Intevac, Inc. Both cameras have been integrated into experimental GV systems. In 2006 and 2007 FOI and FGAN-FOM carried out common field trials using range-gated imaging at 1.5 μm. The first trial was conducted in October 2006 in Älvdalen (Sweden), and the second trial was conducted in October 2007 in Meppen (Germany). The primary goal was system performance comparison of the two different SWIR cameras. The common tests involved investigation, e.g., of long-range identification capability, tracking capability, system performance through obscuration, and also comparison with 3.5 μm thermal imaging. Other investigations included atmospheric and target speckle influence on image quality and 3D imaging.

This paper presents some advanced concepts for GV, including a spectral diversity illuminating technique for speckle reduction, non-line-of-sight imaging, indirect scene illumination, and in particular bistatic configurations. There are only very few papers published concerning bistatic GV imaging [20–23]. Almost all deal with scatter reduction to increase the signal-to-noise ratio. The idea behind our efforts was to work out the advantages of the bistatic versus the common monostatic configuration for scene interpretation by a human observer. This way we made more fundamental investigations of GV imaging, in addition to the pure technology assessment of the two different GV systems.

2. Experimental Setup

A. Equipment

The German range-GV system uses an early Intevac LIVAR Model 120 SWIR camera. This camera is based on the intensified CCD chip TE-EBCCD. The SWIR camera is equipped with two sets of optics developed by the German company Carl Zeiss Optronics GmbH (coated for 1.5 μm) giving field of views (FOVs) of 7 mrad and 14 mrad and instantaneous FOVs of 14 μrad and 27 μrad. A laser range finder from Carl Zeiss Optronics GmbH with a pulse energy of 22 mJ at a wavelength of 1.54μm is used as illuminator. The beam divergence is adjustable with two lenses to 6.7 or 13 mrad. Scopes are used for laser and camera aiming. An IR camera is used for SWIR camera aiming in addition to the scope. The German experimental GV system as of October 2006 is shown in Fig. 1 (right).

The Swedish system for range-GV uses an Intevac LIVAR model 400 c as the SWIR camera. This camera is based on the intensified CMOS chip TE-EBCMOS. The SWIR camera has two sets of optics giving a FOV of 4 or 14 mrad (instantaneous FOV of 10 μrad (diffraction limited) or 24 μrad). A laser range finder from Saab with pulse energy of 17 mJ at 1.57 μm is used as the illuminator. The beam width is adjustable with a zoom lens between 0.5 and 15 mrad. For target detection a long-wavelength IR camera (Saab IRK 2000) is used. The Swedish GV system is shown in Fig. 1 (left).

The most obvious difference between the two GV cameras is the difference in image size, in addition

Fig. 1. Swedish range-GV system mounted on a trailer (left), and the German GV system (right) as of the Älvdalen trial (October 2006).

Fig. 2. Reference targets (panels and vehicles).

to other differences, e.g., in noise characteristics and frame recording rate. The LIVAR 120 camera captures square images of the size 512 by 512 pixels, while the LIVAR 400 c camera captures images of the size 640 by 480 pixels.

B. Reference Targets (Panels and Vehicles)

The reference targets consisted of panels and vehicles. During the Meppen trials we could capture images form a noncombat vehicle such as the dropside cargo truck shown in Fig. 2 (middle) and a military ambulance emblazoned with the Red Cross (cross country ambulance) shown in Fig. 2 (right). In the SWIR range, the vehicle's signature is primarily dominated by the surface material reflectance rather than by object temperature and object surface emissivity.

C. Test Procedures

The Älvdalen measurements enabled long-range imaging up to 10 km and more. A number of test panels (see above) and vehicles and soldiers with weapons were included in the tests. The emphasis was put on comparing the two cameras and studying speckle and atmospheric influence as well as the influence of wetness and dirt on target characteristics. One of the major issues in the Meppen trials was the question of the system performance with respect to different obscurants in the optical path and bistatic measurements. At both institutes, FOI and Fraunhofer FOM, complementary investigations concerning 3D and indirect imaging were made.

3. Monostatic Measurements

A. Medium and Long-Range Imaging Experiments

Figure 3 shows examples of imagery from the FOI system illustrating medium (1–3 km) and long-range (7–10 km) imaging under the influence of different turbulence conditions. In Fig. 3 the single frames (left) in the upper 2 rows can be compared with the result of 25 images stabilized by using some image sharpening processing (right). It has been found through a manifold of experiments that except for very strong turbulence an average of 5–10 frames is sufficient to reduce target and atmospheric influence considerably [6,24].

For stabilized averaging of 5–10 frames the achievable angular resolution of an active imaging system is comparable with the corresponding passive single frame image as illustrated in Fig. 4. The contrast is generally better for the active system owing to reduction of atmospheric scatter by range gating.

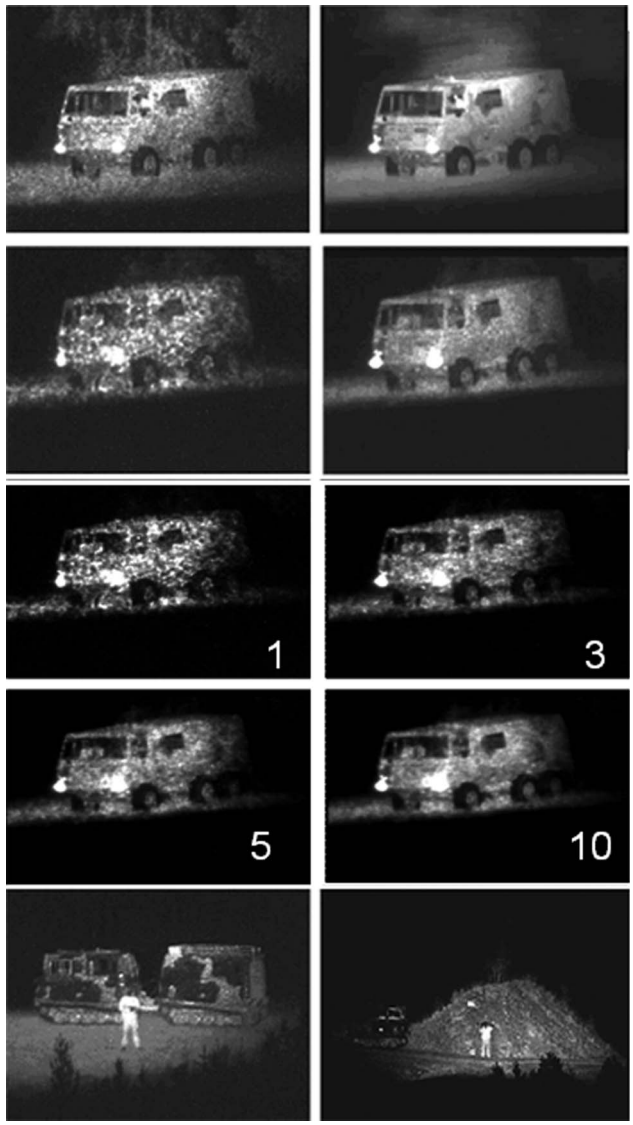

Fig. 3. Single frames (left) and 25 averaged, stabilized or processed frames (right) during low (upper row) and medium (second row) turbulence, range 1.9 km. Rows 3 and 4 show the improvement on integrating 1, 3, 5 and 10 frames for a medium turbulence condition. The last row shows men with weapons at 1 km and 2.5 km, respectively. The focal length was 2000 mm except for images in the lowest row, where the focal length was 500 mm.

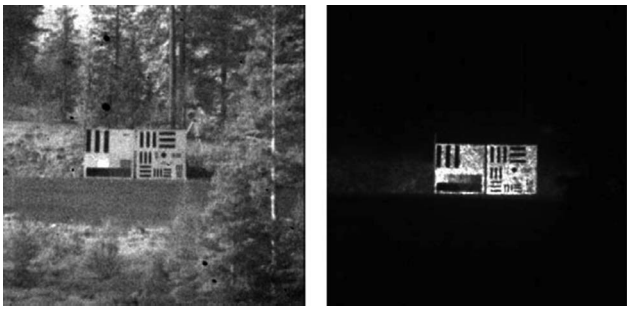

Fig. 4. Comparison of the passive (left) and active (right) operating mode of the LIVAR 120 camera. Test panels at a distance of 1000 m were watched through a 500 mm focal length optics. The number of averaged frames in the right-hand image was 10.

Speckle reduction by broadening the spectral emission of the transmitter. As illustrated above, the quality of range-gated laser images suffers from severe degradations caused by speckle effects due to atmospheric turbulence and target surface roughness. Under medium and severe turbulence conditions mitigating speckle noise has traditionally been accomplished by frame averaging. Another technique is to broaden the spectral line width of the laser transmitter, thus reducing the coherence effects. The speckle contrast C_{sp} as a function of the spectral bandwidth of the illumination source is given by [25]

$$C_{\mathrm{sp}} = \frac{\sigma_I}{\langle I \rangle} = \frac{1}{\sqrt[4]{1 + (2\Delta k \sigma_h)^2}}, \tag{1}$$

where σ_I is the standard deviation of the intensity distribution, Δk the spectral bandwidth given in wavenumbers, and σ_h the standard deviation of the surface roughness. To suppress or eliminate speckle effects (this is equivalent to lowering the contrast) an illumination source with less coherence, i.e., with a very wide spectral bandwidth, is preferable. White-light lasers [26] would represent appropriate illumination sources for this purpose, but the available output power in the SWIR band is insufficient for long-range applications. Averaging several single wavelengths with a wavelength separation $\Delta\lambda$ of the order of

$$\Delta\lambda = \frac{\lambda^2}{2\sigma_h} \tag{2}$$

results in uncorrelated speckle patterns as well and thus in a similar reduction of the speckle noise. Assuming $\lambda = 1.55\,\mu\mathrm{m}$ and $\sigma_h = 10\,\mu\mathrm{m}$, a wavelength separation of about 120 nm is necessary to get uncorrelated speckle realizations. In the case of target surfaces that are tilted with respect to the illuminating beam, speckle patterns tend to decorrelate with increasing tilt angle [27].

In the following sections the performance of range-gated laser imaging using two different illumination techniques will be presented. Compared with conventional illumination operating at a fixed wavelength, the illumination with a wavelength tunable laser source can significantly reduce speckle effects. This part of the work was first presented in [28].

B. Experimental Setup for Speckle Reduction Studies

Two different illuminators were used. One was a flashlamp-pumped Raman-shifted Nd:YAG laser with a wavelength of $1.54\,\mu\mathrm{m}$, a maximum pulse energy of 22.5 mJ, a pulse width of 3 ns, and a maximum pulse repetition rate of 15 Hz. The second illuminator consisted of an optical parametric oscillator (OPO) pumped by the second harmonic (532 nm) of a flashlamp-pumped Nd:YAG laser. The OPO uses a nonlinear crystal for frequency conversion and emits two wavelengths—signal and idler. Tuning the angle of the crystal can shift the OPO output from 0.7 to $1\,\mu\mathrm{m}$ (signal) and from 1.1 to $2.2\,\mu\mathrm{m}$ (idler). The signal output was blocked, and the idler output was used for scene illumination, with a maximum pulse energy of 15 mJ, a pulse width of 9 ns, and a maximum pulse repetition rate of 25 Hz. Images were recorded by an Intevac (LIVAR 400) camera with a detector size of 640 by 480 pixels.

C. Speckle Reduction Measurements

In preliminary experiments we investigated the influence of the two different illuminating sources on the resulting speckle noise. A stone wall of a church at a distance of 450 m was used as a target. The wall was illuminated either with the fixed wavelength of the Raman-shifted Nd:YAG laser (1540 nm) or with different wavelengths by tuning the OPO from 1450 to 1650 nm (step size 20 nm). Figures 5 and 6 show some results of these experiments.

Figure 5(a) shows the wall illuminated at the given wavelength of the Raman-shifted Nd:YAG laser (1540 nm). Fifty consecutive frames were averaged. Because of the frame averaging turbulence speckles are almost suppressed. However, target speckles are still observable. In Fig. 5(b) the OPO was used for illumination. In the experiment the OPO wavelength was kept constant at 1550 nm. Since the spectral bandwidth of the OPO (9 nm) is about 3–4 times larger than the spectral bandwidth of the Raman-shifted Nd:YAG laser (2.5 nm), target speckles are slightly reduced but still observable. In Fig. 5(c) the spectral diversity illuminating technique was applied. At ten different wavelengths five frames were taken and averaged. This technique leads to a clear image where speckles are considerably suppressed. Although for each image the same number of frames were averaged (50 frames each) the image shown in Fig. 5(c) yields the best results. Figure 6 shows the theoretical contrast function C_{sp}, Eq. (1), against the laser linewidth compared with contrast values extracted from Figs. 5(a) and 5(b). The measured values are in good agreement with theoretical calculations. However, the contrast in Fig. 5(c) cannot be described by Eq. (1), since the scene was not illuminated simultaneously but successively by different single wavelengths.

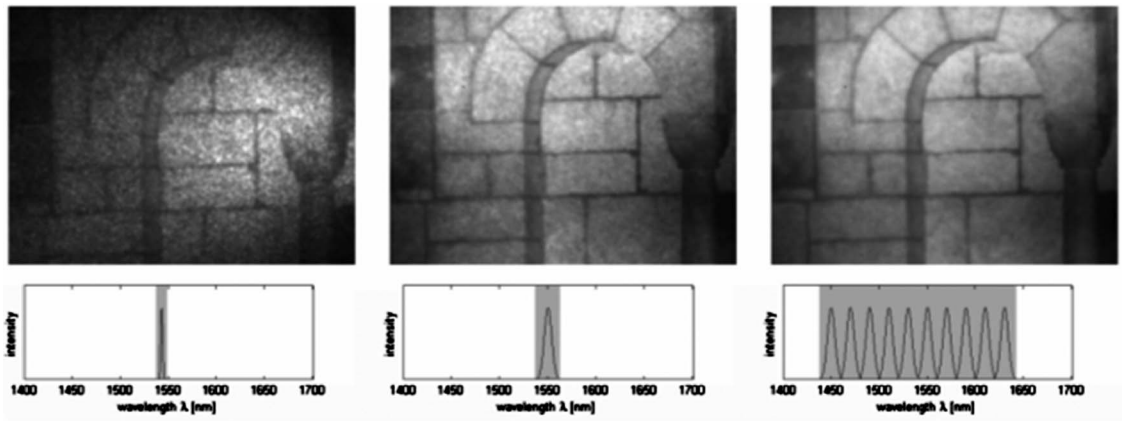

(a) (b) (c)

Fig. 5. Illuminated stone wall of a church at a distance of 450 m and spectral composition of the illuminating laser pulses. (a) Target-induced speckle pattern resulting from illumination with a fixed wavelength of 1.54 μm (Raman-shifted Nd:YAG laser) and a spectral bandwidth of 2.5 nm (50 frames averaged). (b) Reduced target-induced speckle pattern resulting from illumination with a fixed wavelength of 1.55 μm (OPO system) and a spectral bandwidth of 9 nm (50 frames averaged). (c) Resulting image from successive illumination with ten different wavelengths (1450–1630 nm, step size 20 nm). For each wavelength 5 frames were recorded, and the total of 50 frames were averaged.

In Fig. 7 for both illumination techniques 550 frames have been averaged. These measurements clearly show that the target-induced speckle pattern cannot be significantly reduced by frame averaging as long as a small bandwidth illumination source with a fixed wavelength is used. In comparison, averaging 550 frames illuminated by the OPO at different wavelengths leads to a much more homogeneous and almost speckle-free image. This is especially true for a stationary camera and stationary targets. In the case of a moving or vibrating target and/or sensor as well as under severe turbulence conditions, speckle decorrelation occurs [29].

D. 3D Imaging and Speckle Reduction

In the past several different techniques for 3D imaging in range-gated imagery have been presented. Some of them use a large number of sliding gates [13]; other techniques are based on the processing of only two images [14,15]. However, each technique relies on the encoding of the intensity values in range information and suffers from the occurrence of speckle effects. Especially in pixelwise working algorithms, remaining target speckle patterns constrict the depth resolution. The dependence of range accuracy on noise, e.g., speckle noise, was first treated by Andersson [13].

Because speckle appearance also degrades the range accuracy, in our sliding-gate investigations the wavelength shifting illumination technique (as described above) was applied to suppress the speckle noise. A vehicle was positioned at a distance of 2500 m with an orientation of about 30° to the direction of observation. To obtain 3D information of the target the camera gate was set in front of the vehicle and shifted backward in 14 steps with a step size of 1.5 m. For each gate position eight different wavelengths successively illuminated the target. For each wavelength and for each gate position 50 frames were captured. The wavelength range was 1500–1640 nm with a step size of 20 nm. To obtain optimal images for each gate position the entire 400 frames

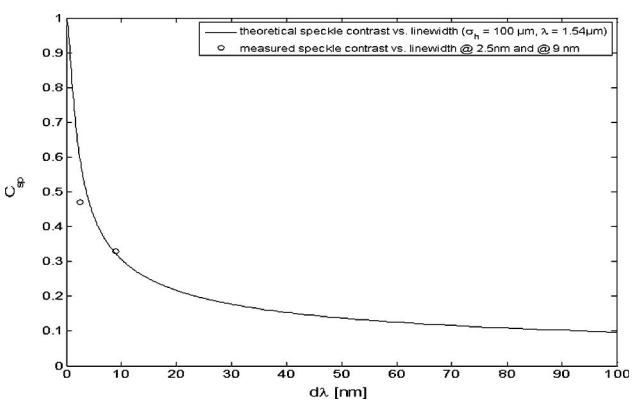

Fig. 6. Theoretical contrast function C_{sp}, Eq. (1), against the laser linewidth compared with the estimated values of Fig. 5 for the two different linewidths 2.5 and 9 nm.

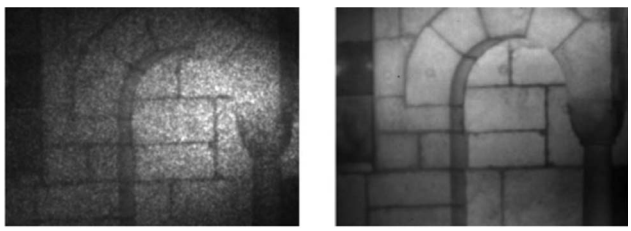

(a) (b)

Fig. 7. (a) Target-induced speckle pattern resulting from illumination with a fixed wavelength of 1.54 μm and spectral bandwidth of 2.5 nm (Raman-shifted Nd:YAG laser). 550 frames were averaged. (b) Same scene as in (a) illuminated with 11 different wavelengths (OPO system). Wavelength range 1450–1650 nm, step size 20 nm. For each wavelength 50 frames were recorded, and the resulting 550 frames were averaged.

(a) (b) (c)

Fig. 8. Camera gate position in front of the target (a), on the target (b), and almost behind the target (c). This subsequence results from tuning the wavelength of the OPO system from 1500 nm to 1640 nm with step size 20 nm. For each wavelength 50 frames were taken. The entire 400 frames for each gate position were averaged.

were averaged. Three representative images of the gate shifting sequence are shown in Fig. 8. They are almost speckle free.

To extract the range for each pixel from the gate shifting sequence different techniques can be applied to the pixel intensity versus time diagram. One is curve fitting using a symmetric, parameterized function describing the convolution of the laser pulse shape and the gate function. As a criterion for the curve fitting error the least squares method was used. The pixel range was derived from the location of the symmetry axis of the fitted curve, Fig. 9(a). In Fig. 9(b) the calculated range of each pixel is illustrated in a gray-scale-coded range image. To estimate the range accuracy, the point cloud of the side panel of the vehicle was calculated and rotated to a top-down view, Fig. 9(c). Owing to a slight curvature of the side panel the considered point cloud has a certain spread in top-down view. So, the error band does not represent the absolute value for the range accuracy with respect to the viewing direction, but the upper limit. Thus, in this case, the range accuracy at a distance of 2500 m is less than 16 cm. This is about a magnitude smaller than the minimum gate step size of 1.5 m.

Under severe turbulence conditions degradation of illumination coherence may occur [12]. This can lead to a strong reduction of speckle effects as well, even when the target is illuminated with a fixed narrowband wavelength source. The advantage of the spectral diversity technique is that it can contribute to image quality and range accuracy under a large number of operational conditions, especially at shorter distances or slant paths (low turbulence conditions).

In our case we tune the OPO manually, which took about 1 min. However, acquisition time can be reduced by use of an automatic tuning system down to a few seconds. The advantage of multiple-wavelength illumination to reduce speckle needs to be balanced against the added complexity, cost, and time required.

1. *Non-Line-of-Sight Imaging Principle*

Time-gated systems open up some potential for indirect viewing via target reflections from walls, windows, vehicles, etc. A capability to see around the corner would be of high interest for defense and military operations in urban scenarios. Some potential applications are illustrated in Fig. 10. A monostatic range-gated system is used to get some hint of target presence behind a street corner or inside a room. The time gating is used to separate the strong first laser return from its vicinity. By scanning a short-range gate after the beam illumination point the hope is

(a) (b) (c)

Fig. 9. (a) Measured intensity distribution of three representative pixels as a function of the gate delay. The solid curves represent the fitted curves. (b) Gray-scale-coded range image of a vehicle at a distance of 2500 m. (c) Top-down view of the point cloud of the vehicle side panel with corresponding error band. The width of this error band with respect to the viewing direction is about 16 cm.

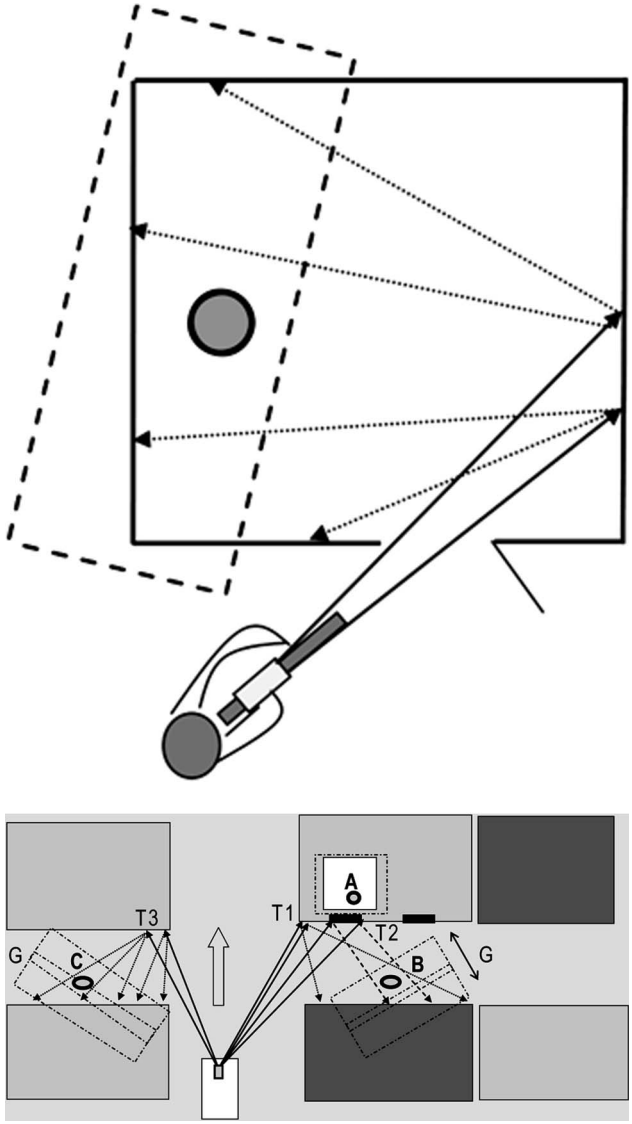

Fig. 10. (Color online) Two illustrations showing different applications of time gating for non-line-of-sight imaging in urban situations. An outdoor street situation is shown in the lower sketch, and a situation inside a building is shown in the upper sketch. In the lower sketch the letters A, B, and C are objects of interest, G represents gate widths, and T1–T3 are different illuminated points on walls or windows.

to detect objects from the illumination at longer ranges. If the beam hits a window or a plane surface giving a specular reflection, the principle should work and could be more advantageous than using a passive electro-optic sensor, where the contrast heavily depends on the surrounding light (sun, street lights, etc.). The most expected advantage for the active illumination is during nighttime.

The critical question for the principle to work is the angular reflection from the illuminated area and the range accuracy of the system, which in turn depends on the gating function and the laser pulse characteristics.

In the case of a single pulse within the gate we obtain the pixel energy from direct illumination from a target at range L_t:

$$E_{\text{target-direct}} = \frac{E_p \eta_r A_r d_{\text{pix}}^2}{\Omega_{\text{laser}} f^2} G(\theta) \frac{\exp(-2\sigma_{\text{ext}} L_t)}{L_t^2}, \quad (3)$$

where E_p is the laser pulse energy, η_r the optical transmission of the filter plus receiver optics, f the focal length of the receiver telescope, A_r the receiver area, σ_{ext} the atmospheric extinction at the laser wavelength, L_t the target range, d_{pix} the pixel size, and $\Omega_{\text{laser}} = \pi \varphi_{\text{laser}}{}^2/4$ the solid laser angle. The normalized reflectivity is $G(\theta)$ per steradian for the angle of incidence θ. The noise equivalent energy per pixel is ENE. The maximum attenuation margin for direct imaging is $M_{\text{dir}} =^{10} \log(E_{\text{target-direct}}/\text{ENE})$ in decibels. If for direct illumination we are using $E_p = 25\,\text{mJ}$, $d_{\text{pix}} = 12\,\mu\text{m}$, $f = 500\,\text{mm}$, $D_r = 9\,\text{cm}$, $\varphi_{\text{laser}} = 10\,\text{mrad}$, $L_t = 100\,\text{m}$, $\sigma_{\text{ext}} = 0.1/\text{km}$, $G(\theta) = 0.05$, $\eta_r = 0.35$ we obtain a margin $M_{\text{dir}} = 62\,\text{dB}$ for $\text{ENE} = 5 \times 10^{-20}\,J/\text{pixel}$.

If we assume that the attenuation from a wall reflection is $A_w(L_{t-w,}\varphi)$ where L_{t-w} is the range between the target and the wall and φ is the angle between the wall and the reflection angle to the receiver, we will have a receiver margin for non-line-of-sight imaging against a wall equal to $M_{\text{indirect}} = (M_{\text{dir}} - 2A_w)$ in decibels. In another program on

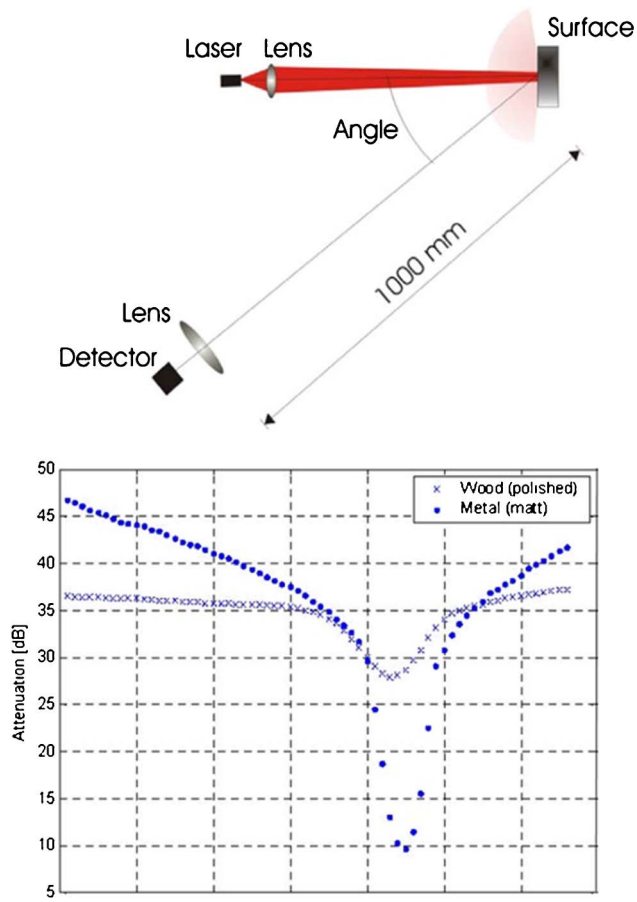

Fig. 11. (Color online) Top, experimental configuration for measuring wall and asphalt reflections at 1 m range. Bottom, attenuation from the wall in terms of loss in the link budget relative to direct illumination [30].

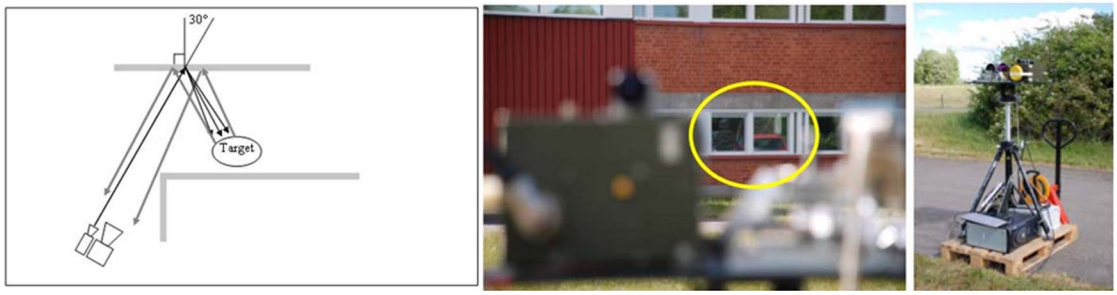

Fig. 12. (Color online) Left, sketch showing the experimental setup for indirect viewing. Middle, windows, with surrounding white painted metal and concrete, and the surrounding brick. Right, equipment with the 1.5 μm laser and the 9 cm diameter receiver ($f = 500$ mm) with an Intevac tube.

non-line-of-sight optical communication we measured the attenuation by wall reflection [30] according to Fig. 11.

E. Example of Experimental Non-Line-of-Sight Imaging

To test the feasibility of non-line-of-sight imaging we performed a simple experiment according to Fig. 12 (left). We will give examples of images for different combinations of laser illuminated and observed area on the wall. For all experiments the laser sensor was at a distance of 90 m from the illuminated wall and looked at a 30° angle relative to the wall plane.

Laser illuminates the glass, receiver FOV covers glass. In this case (Fig. 13) the imaging was relatively easy to obtain as expected. This application is of special interest during nighttime. The time gate can also be placed so that the room behind the window is visible. By using time gating, some capability for looking behind curtains has been demonstrated before [30].

Laser illuminates brick, concrete, and metal, receiver FOV covers glass. In this case the illumination is much weaker, but a glint like target, as shown in Fig. 14 (left), could be observed when illuminating against both brick and concrete. According to the laboratory measurements the minimum attenuation form a brick reflection at 1.5 μm is 35 dB at 1 m range or about 53 dB at 7 m. The loss due to observing via the window reflection is between 10 and 20 dB. For the totally reflecting target the margin might be 70–75 dB for direct illumination; so we can see that the net margin is small.

The license plate at 30 m from the wall could also be observed, although weakly. Throughout the experiment we observed that the gate could not completely shut off the light from the wall's illuminated point until the range was increased to more than 120 m. This stray light was limiting the image contrast.

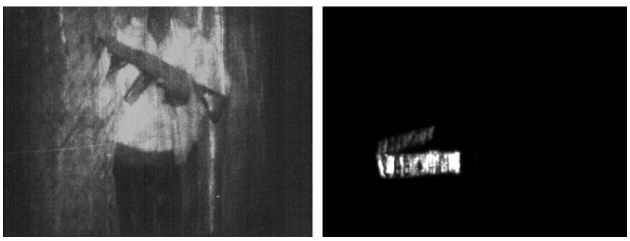

Fig. 13. Left, a man with a gun seen at 20 m from the illuminated wall. Right, a license plate from a car at a 30 m range from the wall.

4. Bistatic Measurements

A. Why Bistatic Measurements?

The disadvantage with an active system is the reduced covertness because of the illuminating laser, which can easily be detected. A conventional GV system is built as a single unit. In that case the laser and the camera are assembled next to each other. Separating the revealing illuminating laser and the camera offers the great advantage of vulnerability reduction for the camera and the operator. The camera location becomes almost undetectable. There is no technical reason why a GV system could not be operated in a bistatic configuration. The laser source and the camera can be separated spatially. The separation distance is determined mainly by the application.

B. Single Camera Configuration

During the Meppen field trials we operated the LIVAR 120 camera in a slave mode waiting for the optical trigger coming from a distant laser illuminator. The laser itself either could operate in a free-running mode with a low-frequency rate or could be triggered, either interactively by the user or through the main GV control software. Fraunhofer FOM was using its GV system in a bistatic configuration in an easy-to-operate mode. For doing that we needed three links (two electrical and one optical) between the operator's console, the camera (which was placed close to the operator), and the laser illuminator, which could be placed anywhere in the field. We successfully recorded some bistatic images from distances of a few hundred meters. In the Meppen field trial we could operate two GV systems. In order to show the single-camera bistatic mode we decided to move the complete German GV system and to use only the Swedish laser for scene illumination. A single optical link was used for the camera trigger picking the laser pulse, and the signal passed through a fiber optics link to the camera. We recorded images of the scene by the same camera from two different locations. For the first group of images we placed the camera as

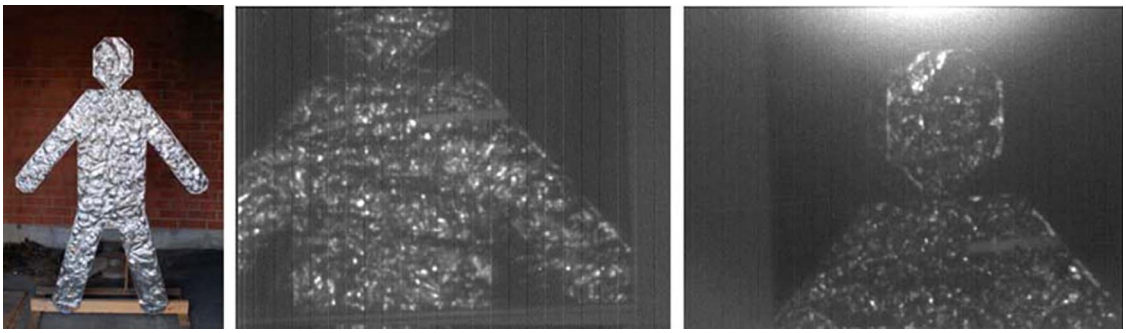

Fig. 14. (Color online) Left, cooperative target (aluminum foil) for experiments when the laser was reflected from brick, concrete, and metal. Middle and right, image of the target when the laser spot illuminated brick and concrete, respectively. The receiver observed the scene from the reflection in a window pane.

close as possible to the illuminating laser (approximately 3 m apart). Later we moved the camera (a few hundred meters) away from the laser and recorded another set images from the same scene.

Two images of noncombat military vehicles are shown in Fig. 15 (upper images) from the first image set. They look pretty much like other images from a conventional (front illuminating scene) GV system. The same vehicles are also shown in Fig. 15 (lower images), but this time recorded from the camera moved to another location. The geometry is shown in Fig. 16 (upper image). The different camera locations are denoted "Camera 1" and "Camera 2." For this experiment Camera 1 and Camera 2 refer to the same camera (in contrast to the two-camera configuration). The different aspects and different scales of vehicles are obvious. There is also a noticeable increase in noise—which indicates that the reflected signal energy reaching the camera is now lower than in the first image set. Both image sets are recorded by the German camera (of course at different times).

Fig. 15. A drop side cargo truck (upper left) and a military ambulance emblazoned with the Red Cross (upper right) as seen by a common GV system (colocated laser and camera). Both images in the lower row show the same targets captured by the same camera after the camera was separated from the laser source. The laser location was the same for all four images; only the camera has been displaced a few hundred meters to the right of the laser for the two lower images.

C. Two-Camera Configuration

During both field trials we usually operated our GV systems independently from each other. This operating mode is sufficient to collect data for system comparison. Having the opportunity to operate two GV cameras at the same time, the idea came up to synchronize both systems. This would enable us to take images by two cameras at the same time from different locations. Because of the very short laser pulse the recorded images would be synchronized in time within a few nanoseconds. In other words, the cameras would be taking snapshots from two locations showing two different aspects of exactly the same scene. In principle, such an operating mode could include more than two cameras also. The Saab laser was used as the scene illuminator. As the Swedish GV system could not be separated, we operated it in the usual GV system operating mode (colocated laser and camera). We moved the German GV system a few hundred meters apart from the other GV illuminator/camera. For the camera synchronization with the Saab laser we used a fiber optics link for the optical pick up—in the way very similar to the way we used it in our single-camera bistatic configuration. Operating two systems in this configuration gave us the opportunity for easy comparison of bistatic measurements versus the conventional operating mode of a single GV system.

Figure 16 (upper image) shows an accurate sketch of the geometric relations during this trial. The viewing distance from the German GV system to the observed scene was about 757 m. Figure 16 (lower left image) shows the Swedish GV system. In front of that system we placed the test panels and the real observation targets. The approximate distance for the observed scenario was about 620 m. Figure 16 (lower right image) shows the German GV system loaded on a truck. The truck itself was placed about 333 m to the right of the Swedish system.

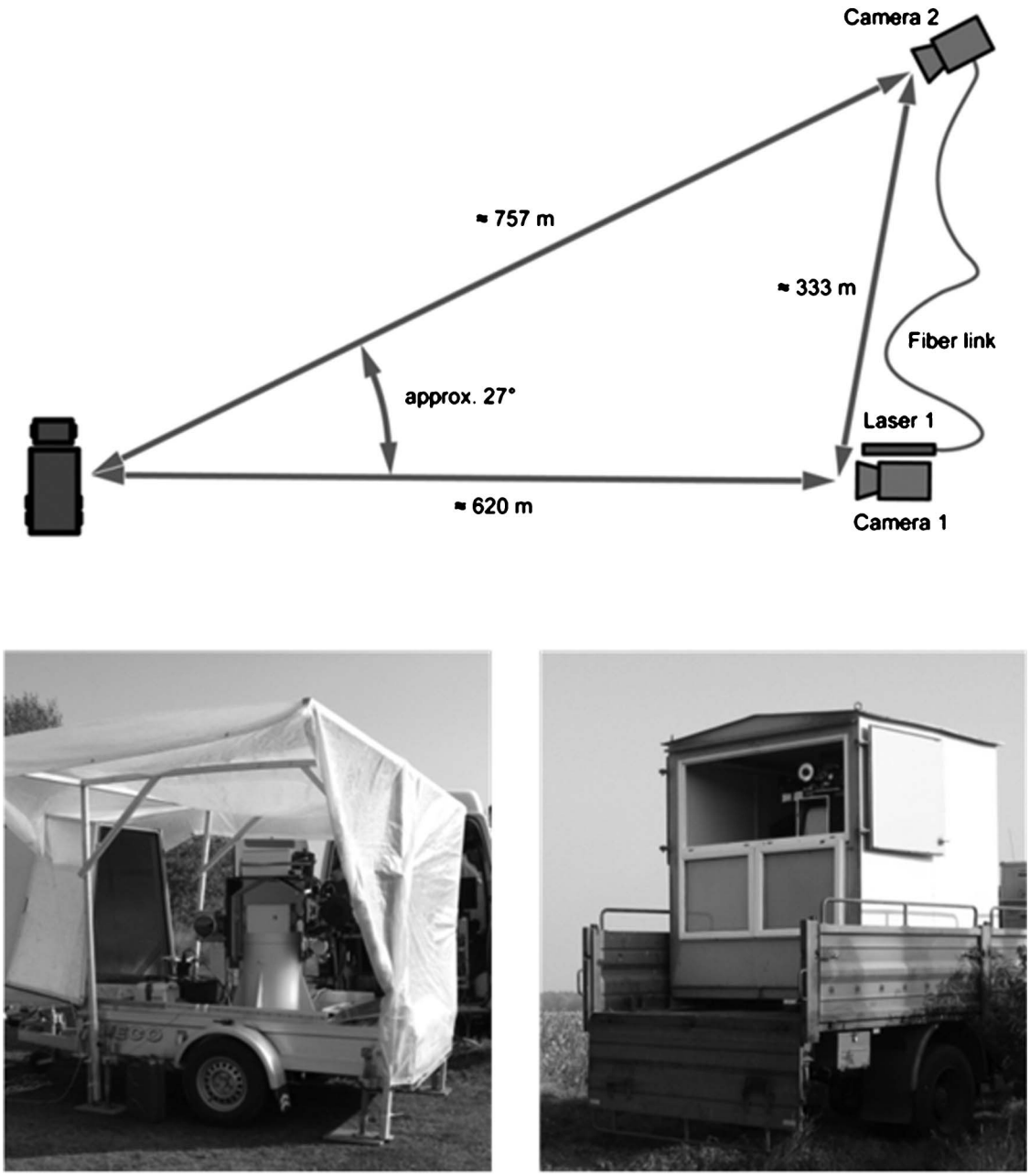

Fig. 16. Top, geometry for the bistatic experiments. Lower left, Swedish GV system, denoted Camera 1 and Laser 1 in the top sketch, was operated in the usual way. Lower right, German GV system, denoted Camera 2, which acted only as a displaced second camera (laser switched off).

We conducted several experiments in this configuration. The idea behind them was trying to find out whether a bistatic operational mode offers any advantages compared with the conventional operating mode. During these experiments we did not change locations of the GV systems—the only thing we changed was the observed scene. Both cameras were equipped with 500 mm focal length objectives to record images of comparable scale. Some of these experiments will be shown in the next sections.

In the next three figures, Figs. 17–19, we show images taken simultaneously by both GV systems (Camera 1 and Camera 2) next to each other. The left images always show the view of the Model 400 camera, while the right images display the view of the Model 120 camera. For all the images of Figs. 17–19 there are some common observations. First, the Model 120 camera captured square images. For this camera the observation area was more distant than for the Model 400 camera. This resulted in different scales (smaller object sizes within the images), despite the fact that we used objectives with the same focal length for both cameras. The right-hand images always show a lower contrast. This is due to the bidirectional reflection distribution function characteristics of materials. Usually an off-axis camera collects less power reflected from objects than an on-axis camera. To compensate for that power loss,

Fig. 17. Images showing strong reflections in the frontal view (on-axis view; left-hand images) and images showing the remaining reflections from a side view (off-axis view, right-hand images). Only a few parts of the vehicles show glossy reflection characteristics in both viewing directions.

we had to increase the camera sensitivity, which on the other hand resulted in added noise. The increased noise within those images is easy noticeable.

1. *Retroreflections*

One of the unavoidable and obvious effects that can always be seen in images captured by GV systems is retroreflection. Some parts of an illuminated object appear very bright. There might be several causes, such as a reflector in a lamp housing or materials with a high specular reflection characteristic (glossy materials).

To investigate these effects we placed the vehicles in different orientations and recorded a few images. The results are shown in Fig. 17. It should be noted that the lights of the vehicles were turned off. Strong retroreflections can be seen in the left-hand images. Please refer also to Fig. 15, which shows the same vehicles from the side. Figure 15 (upper images) also displays strong retroreflections in the side views. In the off-axis images (Fig. 15, lower images and Fig. 17, right-hand images) retroreflections (from lamps, license plates, etc.) are limited, and there is no longer noticeable signal saturation.

2. *Shadow Casting*

Most GV systems are operated in an interactive mode, and the captured scene is prepared for display to the operator or observer. Scene interpretation of a natural scene by humans is a complex task. This is true even in the real 3D world, and is much more difficult if it is based only on 2D images of a real 3D scene. The interpretation of 3D scenes can be supported by additional cues due to appearance of shadows. Every active imager illuminates the scene; therefore shadows will always be there. But because of the on-axis image capturing, they would be hardly ever seen.

It is mainly the lack of observable shadows in the images that causes another effect, too. A captured scene appears often flat when the image was taken from nearly the same location from which the scene was illuminated. This is a well-known fact from facial or portrait photography and from computer graphics. Missing shadows and weak shading changes (on curved surfaces) are the main reason.

We captured a few images from a dynamic scene in bistatic mode to see some shadow effects. The results are shown in Fig. 18. The acting person was casting shadows on the ambulance vehicle in both situations. In the off-axis image (Fig. 18, lower right-hand image) the illuminated person can be seen in front of another shadow, cast by the cabin of the front truck on the ambulance vehicle. In this scene the acting person can be seen much easier in the off-axis images than in the on-axis images. In this particular case this is due to local contrast enhancement between the foreground image (person shape) and the surrounding background image content.

In similar situations, like those shown in Fig. 18, there are two hints that can be used for the situation interpretation, the illuminated object itself and its shadow. In Fig. 18 (right-hand images) detailed hints on the person's pose can be derived from the observable shadows. There is also one small drawback—the scene interpretation of a GV image could be confused a bit because object parts covered by shadows (e.g., unilluminated object parts) do appear very similar to the scene parts that are out of the gate. These different image areas (which both appear

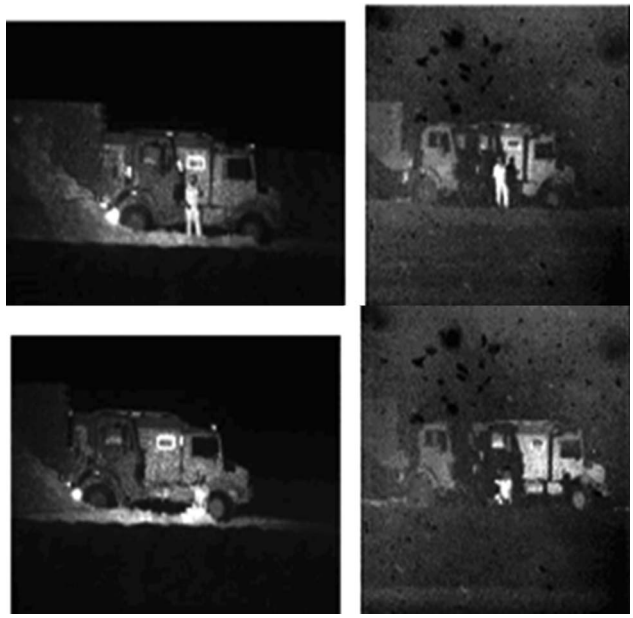

Fig. 18. Left, images showing two different situations as seen by a conventional GV system. Right, in the side-view (off-axis) images shadows of the targets appear.

black) cannot be distinguished easy. But the advantage of the recognizable shadows might outweigh this minor confusing effect much more.

3. *Indirect Illumination*

In bistatic operating mode, we are, e.g., mainly controlling the location (and the gate time) of the camera only. The illuminating laser might be running free and could be operated unattended. The laser could also be used in a much more controlled way and be relocated or reoriented if necessary. Additionally the laser beam itself could also be modified. One idea investigated in the Meppen trial concerned the primary object reflections as secondary illumination source and trying to record the secondary object reflections. A precondition for doing that measurement was successful operation in the bistatic mode. In the usual operating mode GV systems capture mainly primary object reflections. Depending on the scene geometry and material properties, there are of course secondary reflections, also. But the laser energy reflected by the secondary reflections is much lower than from the primary reflections. In the Meppen trial we prepared a specific scenario in order to have controlled secondary reflections.

Figure 19 shows a specific scene we captured in bistatic mode. In both off-axis images (Fig. 19, right-hand images) most scene details captured come from primary reflections. The only noticeable secondary reflections come from the person behind the truck. In the usual operating mode of a GV system (on-axis imagery) that person could not be illuminated directly and moreover, due to the on-axis camera alignment, that person could not be seen directly.

Fig. 19. Same scenario illuminated by the laser source whose divergence was adapted to the FOV of the camera (upper left image) and with decreased divergence (lower left image) in order to increase the reflected laser power. This makes indirect illumination more recognizable in the off-axis images (right-hand images). Sensitive cameras are able to capture secondary reflections from objects being illuminated indirectly. In the lower right-hand image a person can be recognized behind the truck. This person was completely hidden by the truck in the on-axis views. This person cannot be recognized in the on-axis images.

5. Discussion and Conclusions

Preliminary analysis of the two measurement campaigns have been made indicating that range-gated imaging systems working at 1.5 μm can be used for long-range target classification offering an advantage in angular resolution when compared with a mid- or long-wavelength IR system with about the same size aperture. Atmospheric speckles dominate for horizontal long-range paths, and target-induced speckles at closer range. The way to mitigate speckle noise is frame averaging and/or spectral diversity. Note that image stabilization algorithms in general have to be implemented to reduce image jitter induced by the atmosphere or the system movement.

The presented spectral diversity illuminating technique using a tunable OPO results in much more homogeneous range-gated images with considerably reduced speckle patterns. Moreover, the accuracy of the calculated range images is significantly improved.

Target detection and especially classification is simplified with a range-gated technique that can use both direct target illumination and silhouette detection. Glint detection is a strong indicator of man-made targets. However an IR system has a much wider search capability, which makes a combination of GV and IR very natural. SWIR imaging is more robust than thermal imaging, and its appearance reminds one more of a TV image, making it easier to interpret than a thermal image.

In certain conditions GV systems penetrate obscurants or vegetation and thus uncover certain camouflage measures better than thermal IR. The capability of looking through transparent media (like windows) could be very advantageous in distinct situations. The range capability of a GV system makes absolute target dimensions easily extractable, and 3D reconstruction can be accomplished from image sequences. In addition a GV system could be favorable for target tracking owing to its enhanced capability to separate target and background. A silhouette extraction cannot be done in passive IR imagery.

The non-line-of-sight imaging using a monostatic system offers interesting capabilities in the case of specularlike reflecting objects as shown in our results. Examples of such surfaces are windows in buildings and cars, traffic signs, and vehicle surfaces. Important to overcome the large losses in the reflection processes are system parameters such as laser energy, receiver aperture, and detector sensitivity combined with short and distinct gating properties. By using a sliding gate the interior behind a window

can be scanned, followed by images of the vicinity concealed by the corner.

In a bistatic configuration the operator (and the camera) could be positioned far away from the laser illuminator. This way an enemy spotting the laser would not spot the camera. The appearance of shadows in bistatic configurations can simplify any scene interpretation by an observer. Depending on the scene content, local contrast enhancement could happen (a person in front of a shadow). Also, a reduction of retroreflections is observed. In a bistatic configuration the dazzling risk to the camera is less than for the conventional GV system configuration. Since in bistatic configurations the scenery is illuminated under tilt angles, bistatic images show a lower signal-to-noise ratio due to the bidirectional reflection distribution function characteristics of materials. Additionally laser speckles tend to decorrelate, leading to a reduced speckle contrast.

There are also some challenges for the bistatic configurations. The most important one is the accurate aiming of the laser (and of the camera) at the object of interest. A trade-off between laser energy and beam divergence has to be considered. Beam shaping could be an option. Fast communication links between all the distributed components, cameras, and laser sources should be available. This communication can be done by picking up the laser reflections from the target area from the illuminating laser and synchronizing the receiver gate with the illuminating laser pulse emission. The reflectivity generally falls off for higher angles of incidence, which often reduces the signal-to-noise ratio when compared with the monostatic case. On the other hand, the sometimes disturbing strong glints are reduced in the bistatic case, as is the speckle contrast for tilted surfaces.

We acknowledge financial support by the Swedish Defence Materiel Administration (FMV) and financial support by the Federal Office of Defense Technology and Procurement (BWB) from Germany.

We sincerely appreciate valuable assistance by the people from Älvdalens Skjutfält in Trängslet, Sweden, and Bundeswehr Technical Center for Weapons and Ammunition (WTD 91) in Meppen, Germany, during the field trials. We thank Frank Gustafsson and Kjell Karlsson from FOI as well as Uwe Adomeit, Richard Frank and Frank Willutzki from FGAN-FOM for operating all the necessary equipment. The support of Pierre Andersson during the Älvdalen trial is especially appreciated.

References

1. A. F. Milton, G. Klager, and T. Bowman, "Low cost sensors for UGVs," Proc. SPIE **4024**, 180–191 (2000).
2. M. Turner, "Standoff precision ID in 3-D," www.darpa.mil/ipto/programs/spi3d/spi3d.asp.
3. A. Weidemann, G. R. Fournier, L. Forand, and P. Mathieu, "In harbor underwater threat detection/identification using active imaging," Proc. SPIE **5780**, 59–70 (2005).
4. D. Bonnier, S. Lelièvre, and L. Demers, "On the safe use of long-range laser active imager in the near-infrared for homeland security," Proc. SPIE **6206**, 62060A (2006).
5. Night vision systems, www.turn.ru/porducts/index.htm
6. O. Steinvall, P. Andersson, M. Elmqvist, and M. Tulldahl, "Overview of range gated imaging at FOI," Proc. SPIE **6542**, 654216 (2007).
7. I. Baker, D. Owton, K. Trundle, P. Thorne, K. Storie, P. Oakley, and J. Copley, "Advanced infared detectors for multimode active and passive imaging applications," Proc. SPIE **6940**, 6902L (2008).
8. J. Fortin, E. Thibeault, and G. Pelletier, "Improving the protection of the Canadian light armored vehicle using a laser based defensive aids suite," J. Battlefield Technol. **9**(3), 13–18 (2006).
9. D. Bonnier and V. Larochelle, "A range-gated active imaging system for search and rescue, and surveillance operations," Proc. SPIE **2744**, 134–145 (1996).
10. H. Larsson, O. Steinvall, T. Chevalier, and F. Gustafsson, "Characterizing laser radar snow reflection for the wavelengths 0.9 and 1.5 μm," Opt. Eng. **45**, 116201 (2006).
11. R. G. Driggers, R. H. Vollmerhausen, N. Devitt, C. Halford, and K. J. Barnard, "Impact of speckle on laser range-gated shortwave infrared imaging system target identification performance," Opt. Eng. **42**, 738–746 (2003).
12. O. Steinvall, P. Andersson, and M. Elmqvist, "Image quality for range-gated systems during different ranges and atmospheric conditions," Proc. SPIE **6396**, 6396-07 (2006).
13. P. Andersson, "Long-range three-dimensional imaging using range-gated laser radar images," Opt. Eng. **45**, 034301, 1–10 (2006).
14. M. Laurenzis, F. Christnacher, and D. Monnin, "Long-range three-dimensional active imaging with superresolution depth mapping," Opt. Lett. **32**, 3146 (2007).
15. Z. Xiuda, Y. Huimin, and J. Yanbing, "Pulse-shape-free method for long-range three-dimensional active imaging with high linear accuracy," Opt. Lett. **33**, 1219–1221 (2008).
16. O. Steinvall, T. Chevalier, P. Andersson, and M. Elmqvist, "Performance modeling and simulation of range-gated imaging systems," Proc. SPIE **6542**, 6542-18 (2007).
17. R. L. Espinola, E. L. Jacobs, C. E. Halford, R. Vollmerhausen, and D. H. Tofsted, "Modeling the target acquisition performance of active imaging systems," Opt. Express **15**, 3816–3832 (2007).
18. M. P. Strand, "Imaging model for underwater range-gated imaging systems," Proc. SPIE **1537**, 151–160 (1991).
19. R. G. Driggers, J. S. Taylor, and K. Krapels, "Probability of identification cycle criterion ($N50/N90$) for underwater mine target acquisition," Opt. Eng. **46**, 033201 (2007).
20. M. P. Strand, "Bistatic underwater optical imaging using AUVs," Ocean Optics & Biology (OB) FY08 Annual Reports, Office of Naval Research 875 North Randolph Street, Arlington, Va. 22203-1995 (2008).
21. J. Lin, H. Mishima, T. D. Kawahara, Y. Saito, A. Nomura, K. Yamaguchi, and K. Morikawa, "Bistatic imaging lidar measurements of aerosols, fogs and clouds in the lower atmosphere," Proc. SPIE **3504**, 550–557 (1998).
22. B. M. Welsh and C. S. Gardner, "Bistatic imaging lidar technique for upper atmospheric studies," Appl. Opt. **28**, 82–88 (1989).
23. W. R. Watkins, D. H. Tofsted, V. G. CuQlock-Knopp, J. B. Jordan, and M. M. Trivedi, "Active imaging applied to navigation through fog," Proc. SPIE **3749**, 750 (1999).
24. O. Steinvall, H. Larsson, F. Gustafsson, D. Letalick, T. Chevalier, Å. Persson, and P. Andersson, "Performance of

3-D laser radar through vegetation and camouflage," Proc. SPIE **5792**, 129–142 (2005).
25. J. C. Dainty, *Laser Speckle and Related Phenomena* (Springer Verlag, 1975).
26. D. A. Orchard, A. J. Turner, L. Michaille, and K. R. Ridley, "White light lasers for remote sensing," Proc. SPIE **7115**, 711506 (2008).
27. C. E. Halford, A. L. Robinson, R. G. Driggers, and E. L. Jacobs, "Tilted surfaces in shortwave infrared imagery: speckle simulation and a simple contrast model," Opt. Eng. **46**, 1–11 (2007).
28. B. Göhler, P. Lutzmann, and G. Anstett, "3D imaging with range gated laser systems using speckle reduction techniques to improve the depth accuracy," Proc. SPIE **7113**, 711307 (2008).
29. J. H. Shapiro, "Correlation scales of laser speckle heterodyne detection," Appl. Opt. **24**, 1883–1888 (1985).
30. P. Sakari and M. Pettersson, "Optical communication in urban areas, focus on non line-of-sight optical communication," Reps. PB2004-104593, FOI-R-0944-SE (Swedish Defence Research Establishment, Sept. 2003), available from National Technical Information Service (NTIS).